Virtual Signal Integrity Test on Shielded/Unshielded Twisted-Wire Pairs in Reverberation Chambers Under Realistic Industrial Constraints

Sahand Rasm, Guillaume Andrieu, Alain Reineix, Remi Tumayan

HAL Id: hal-03850607

https://unilim.hal.science/hal-03850607

Submitted on 14 Nov 2022

"Virtual" Signal Integrity Test on Shielded/Unshielded Twisted-Wire Pairs in Reverberation Chambers Under Realistic Industrial Constraints

Sahand Rasm, Guillaume Andrieu, *Senior Member, IEEE,* Alain Reineix, *Member, IEEE,* and Rémi Tumayan

Abstract—A recent method able to perform "virtual" signal integrity test on twisted-wire pairs (shielded or not) using a bulk current injection setup is, in a first part, extended successfully to the case of reverberation chamber tests in order to deal with a higher frequency range. The method, allowing in post-processing to superimpose the effect of the measured disturbance (calculated from S-parameter measurements) to a useful signal generated numerically, is proven to be independent of the measurement conditions (position of the antenna, RC quality factor for instance) and is able to easily consider the electromagnetic field uncertainty. In a second part, the method is improved through the use of full-wave numerical simulations in order to deal with realistic industrial constraints. The method can therefore be applied on twisted wire pairs of any length and connected to frequency-dependent termination loads of any values. The method allows to predict accurately (up to 2 GHz in the paper) the signal integrity of any communication protocol and could help therefore industrial to decide if a shielded version is necessary or not. An example of bit-error-rate prediction is finally done on a 100BASE-T1 fast Ethernet protocol signal on two shielded/unshielded twisted wire pairs.

Index Terms—Bit-error-rate, common-mode, common-mode rejection ratio, common-mode/differential-mode conversion, differential-mode, Ethernet cable, immunity, radiated susceptibility test, reverberation chamber, shielded cable, shielding, signal integrity, twisted-wire pairs.

I. INTRODUCTION

T HE continuous growth of the number of sensors and the volume of data to be transmitted within an automobile or an aircraft requires cable networks supporting increasing data rates. In the automotive industry, it is probable than twisted-wire pairs (TWPs) contained in Ethernet and LVDS cables will probably be the most commonly used cables for high-speed wired communications [1]. Even if these high-speed networks solve the problem of data throughput, the study of their immunity to an electromagnetic (EM) interference becomes more and more fundamental for the automotive industry [2]–[4].

Instead of limiting the analysis to transfer impedance [5]–[8] or shielding effectiveness [9]–[11] results, the authors have

proposed recently [12] a method in order to verify "virtually" the signal integrity of cables (and particularly TWPs) from S-parameter measurements and thanks to a bulk current injection (BCI) setup [13]. Indeed, the linearity of these measurements allows the differential-mode (DM) voltage related to a constant-wave (CW) disturbance of any amplitude to be calculated at a given frequency for any common-mode (CM) current created on the cable (shielded or not) by the injection probe and for different values of CM-to-DM conversion [14]–[16].

This method is in this paper extended to the case of radiated susceptibility (RS) tests performed in reverberation chambers (RC) in order to increase the frequency range of the potential disturbance until a few GHz (2 GHz in the paper without loss of generality). It is in particular shown that the uncertainty related to the average strength of the electric field can be easily taken into account. In a second step, the method is improved, thanks to the help of numerical simulations, in order to consider more realistic industrial constraints, for instance frequency-dependent termination loads on TWPs of any length.

The paper is organized as follows. The method is extended in section II to the case of RS tests performed in RCs. This sections contains in particular a description of the required measurement setup and of the post-processing approach as well as some results showing the interest of the approach. In section III, the method is improved from full-wave simulations of the RC using the plane wave spectrum approach in order to treat more realistic constraints. This is done in particular thanks to the help of numerical simulations using a full-wave software.

II. EXTENSION OF THE METHOD TO RC TESTS

A. Brief Reminder of the Method With a "BCI-like" Setup

The principle of the method proposed recently (and briefly summarized here) [12] consists in verifying "virtually" the signal integrity of a useful signal transmitted using a TWP thanks to an experimental setup inspired of the BCI one. The term "virtually" means that the useful signal $s_u(t)$ is not measured but generated numerically (for instance using a MATLAB-like software) in the time-domain. The signal integrity analysis being made in post-processing, the useful signal can therefore represents any communication protocol.

Of course, one understands here that complex communication protocols are handled at a cost of a more complex post-processing program. The disturbance signal $s_p(t)$, which is added to the useful signal also in the time domain to obtain the disturbed signal $s_d(t)=s_u(t)+s_p(t)$ is related to the S-parameter measurements collected with the "BCI-like" setup. Indeed, it is a sinusoidal CW signal calculated at a frequency f_p, provided that the S-parameter measurements have been performed at this particular frequency. Thanks to the linearity of the problem and as classically done in BCI tests, the amplitude of $s_p(t)$ can be calculated for any value of the constant (with respect to the frequency) current I_{bci} generated by the injection probe at the cable termination, i.e. where the equipment is supposed to receive the useful signal. This current I_{bci}, being either the CM current generated on an unshielded TWP or the current flowing along the shield for a shielded one, would be obtained (but it is not required in the method) after varying for each frequency the forward power P_f supplying the injection probe. The method leads to an in-depth analysis of the received signal and allows comparing in particular the difference obtained if the TWP is shielded or not. All the analysis is made numerically during the post-treatment with the noticeable exception of the fast (i.e., a few minutes) S-parameter measurements.

B. Differences between BCI and RC Tests

As mentioned in the introduction, the method is in this paper extended to the case of a RS test performed in a RC [17]–[19]. The aim is to extend the realization of a "virtual" signal integrity test towards higher frequencies of a few GHz, BCI tests being generally limited to 400 MHz as specified in BCI standards (mainly in reason of the non linearity of the injection probe [15]). Thus, two major differences between BCI and RS tests have to be clearly highlighted.

Even if a BCI test can be performed for different locations of the injection probe around the TWP, a RS test in RC is repeated at a given frequency for a large number N of stirring configurations, for instance the number of mode stirrer positions. It is therefore interesting to use the information obtained for all these configurations in the subsequent virtual signal integrity test. Finally, in a BCI test, the metric quantifying the disturbance magnitude is the current I_{bci} defined above, whereas in a RC it is a metric related to the magnitude of the EM field strength. In this paper, we have chosen to define the magnitude disturbance generated in the RC through the average total electric field strength, i.e. $\langle|E_T|\rangle$, the metric considered as the most reliable one [17]–[19].

C. Required Measurement Setup

1) General Characteristics of the Setup: The required measurement setup to apply the method in a RC is sketched in Figs. 1-2. The emitting antenna is connected to the port 1 of a vector network analyzer (VNA) located outside the RC. The TWP (shielded or not) runs at a constant height above a metallic ground plane and is supported by two metallic brackets. Both wires of the TWP are connected at each extremity to a dedicated PCB (which is, as proven later,
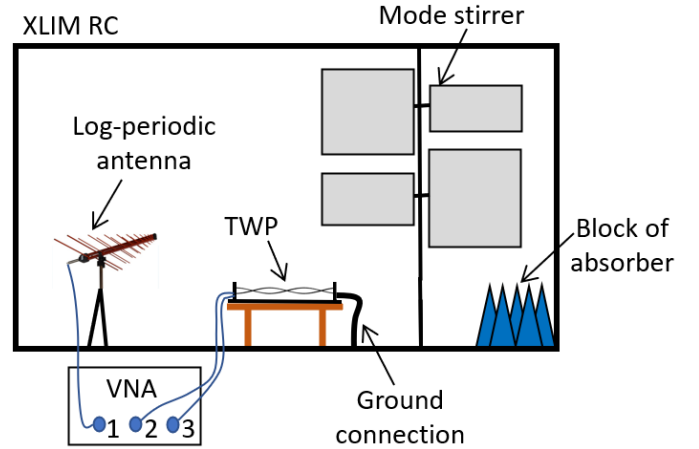

Fig. 1. Schematic description of the required measurement setup. A 2-port VNA is also usable after modifying the successive ports to measure and inserting a 50 Ω impedance on each unconnected port. The presence of the block of absorber is optional.
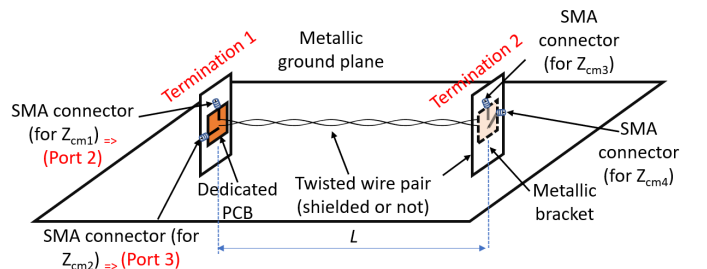

Fig. 2. Schematic description of the cable under test.

perfectly balanced on the frequency range of interest) provided by the cable supplier and equipped of SMA connectors. The aim is to measure the CM voltage induced between both TWP conductors and the ground at a given termination of the TWP. Therefore, at the cable termination called "Termination 1", the port 2 of the VNA links the extremity of the first TWP wire (through the dedicated PCB) to the ground reference, port 3 doing the same for the other wire. At the other termination (i.e. "Termination 2") of the TWP, the other PCB allows two CM loads, defined as Z_{cm3} and Z_{cm4}, to be inserted. After carrying out these measurements for N stirring configurations, all the other steps of the method are done in post-processing as described later.

2) Specific Characteristics of the Setup: Specifically, the measurements related to the results shown in this paper have been performed in the RC of the XLIM laboratory (3.75 m long, 2.45 m wide, 2.46 m high, volume $V \approx 22.6$ m^3, with a theoretical fundamental resonance $f_0 \approx 73$ MHz) as shown in Fig. 3. The RC is equipped with a rotating mode stirrer made of 8 rectangular metallic plates of 60 by 40 cm^2 dimensions [20]. The emitting antenna is a broadband log-periodic antenna. Two different loading conditions of the RC have been considered: when no absorber is inserted in the RC (i.e. the "unloaded" configuration) and when the RC is loaded with a block of 30 pyramidal absorbers (PA) (i.e. the "loaded" configuration), each PA having a squared ground surface of 100 cm^2 with a height of 30 cm. The average mode
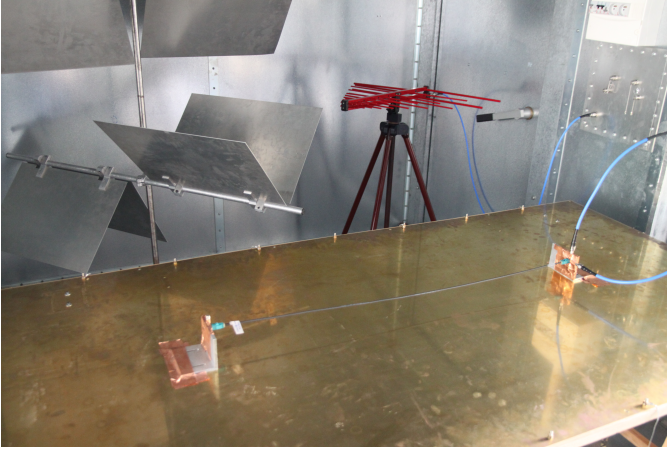
Fig. 3. Picture of the experimental setup in the XLIM RC. The TWP running above the metallic ground plane is shown at the foreground while the log-periodic antenna and the rotating mode stirrer are in the background.
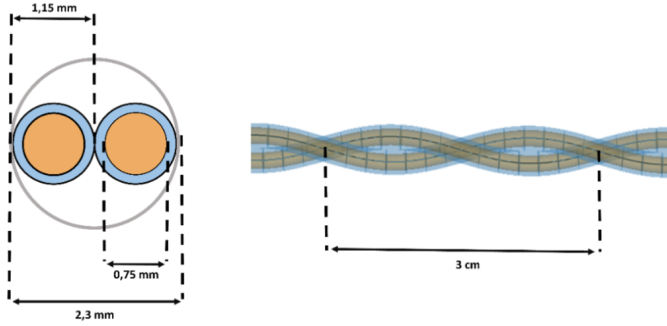

Fig. 4. Schematic description of the cross-section geometry of the unshielded TWP (on the left) and of its longitudinal view (on the right). Note that only 1 TWP is represented.

bandwidth (defined as $\Delta_f = f/Q(f)$ [21] and and assumed to be constant on the considered bandwidth) related to these two loading configurations is respectively of 0.5 and 0.9 MHz.

The Ethernet cables tested in this study are all made of 4 conductors constituting 2 TWPs of 50 cm, 75 cm and 1 m length (which is the typical cable length used in BCI tests), the second TWP being left unconnected in all our measurements. For each given length, an "unshielded" version and a double shielded one (designated as the "shielded" TWP) surrounded by an aluminum foil and a braided shielding also made of aluminum have been used and connected, through the dedicated PCB, to two metallic brackets of 10 cm width and 8 cm height. As described in Fig. 4 for the unshielded TWP, each TWP is made with copper wires (of radius 0.375 mm) and polyethylene coatings (of thickness 0.2 mm and assumed to have a dielectric permittivity of 2.3) while an outer dielectric coating surrounds both wires. After accurately examining one TWP, the length of a twist is roughly 3 cm. As mentioned by the supplier, both TWPs have a 100 Ω DM characteristic impedance. The distance of the TWP with respect to the ground equals 5 cm in all the experiments we have made.

Measurements have been done using a 4-port VNA on the frequency range from 0.2 to 2 GHz over 1801 frequencies linearly stepped (i.e. δ_f = 1 MHz) for 100 mode stirrer positions
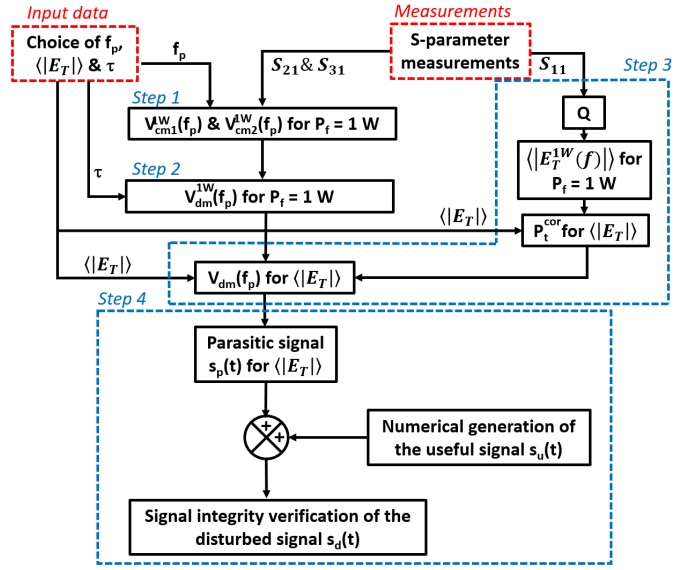

Fig. 5. Flowchart presenting the different steps of the method. This process can be repeated for each set of input data (i.e. f_p, I_{bci} and τ) of the parasitic signal $s_p(t)$ and for each stirring configuration (i.e. each mode stirrer position for a mechanically stirred RC).

(i.e. rotation of 3.6^o between two successive positions). The measurement time for each configuration is about 20 minutes (once the VNA is calibrated). It is assumed that the method presented after could work at higher frequencies than 2 GHz.

D. Detailed Description of the Method in RC

The flowchart summarizing the different steps of the method is presented in Fig. 5 for a frequency of the sinusoidal parasitic signal f_p (i.e. the first input data to be inserted in the post-processing program).

According to the theory developed in [12], each S_{k1} measurement (with k being 2 or 3) measured for one given position of the rotating mode stirrer allows in the step 1 the CM voltage $V_{cm(k-1)}$ at termination 1 of one conductor of the TWP to be calculated (at any frequency f_p where the S-parameters have been measured) for a forward power P_f of 1 W supplying the antenna

$$V_{cm(k-1)}^{1W}(f) = \frac{S_{k1}(f)}{2}\sqrt{\frac{8.\,Z_0.P_f}{1-|S_{11}(f)|^2}}. \qquad (1)$$

The second step of the method consists in calculating the differential voltage $V_{dm}(f_p)$ induced by the disturbance at the frequency f_p for the same forward power. As extensively described in [12], the terminal impedances of the TWP being perfectly balanced (and equals to 50 Ω), it is assumed that $V_{dm}(f_p)$ is almost null. To introduce fictitiously a CM-to-DM conversion of the disturbance in order to represent realistic cases, a CM rejection ratio (CMRR) τ [12,14]–[16] (in dB) is introduced as follows

$$\tau = 20\log_{10}\left(\frac{\left|V_{cm}^{1W}(f_p)\right|}{\left|V_{dm}^{1W}(f_p)\right|}\right) \qquad (2)$$

with $|V_{cm}|$ the average of $|V_{cm1}|$ and $|V_{cm2}|$.

Therefore, the choice of τ directly leads to the differential voltage $V_{dm}^{1W}(f_p)$ induced at termination 1 of the TWP for an injected power of 1 W. A high τ value involves a low DM disturbance which is preferable from a signal integrity point of view.

In the third step of the method, $V_{dm}^{1W}(f_p)$ has now to be corrected in order to consider that the average total electric field strength $\langle|E_{\mathrm{T}}|\rangle$ is constant on the entire frequency range, as generally done in RS tests performed in RC. This is done through the determination of the RC quality factor Q, which quantifies the ability of the RC to store the energy, from the S-parameter measurements [22]. For instance, using the reflection coefficient of the antenna (i.e. S_{11}), Q is obtained easily

$$Q = \left\langle |S_{11} - \langle S_{11}\rangle|^2 \right\rangle \frac{Z_0 \omega \varepsilon V}{(\lambda^2/4\pi)\left(1 - |\langle S_{11}\rangle|^2\right)^2 \eta^2} \tag{3}$$

where Z_0 is the wave impedance, ω the pulsation, λ the wavelength, η the efficiency of this antenna, ϵ the dielectric permittivity of the vacuum and V the total volume of the RC. Once Q is known, $\langle|E_{\mathrm{T}}|\rangle$ can then be estimated for any transmitted power P_t to the antenna (with $P_t = P_f\left(1 - |\langle S_{11}\rangle|^2\right)$) as follows

$$<|E_T|> = \sqrt{\frac{QP_t}{\omega\varepsilon V}}\frac{15}{16}\sqrt{\frac{\pi}{3}} \tag{4}$$

where the term $15/16\sqrt{\pi/3}$ is related to the inequality $\sqrt{<|E_{\mathrm{T}}|^2>} \neq <|E_{\mathrm{T}}|>$ [23]. In other terms, the aim here is to compute the required (corrected) transmitted power $P_t^{cor}(f_p)$ in order to obtain the desired value of $\langle|E_{\mathrm{T}}|\rangle$ within the RC at each frequency of interest.

It is therefore easy to calculate $V_{dm}(f_p)$ which would be measured for the desired value of $\langle|E_{\mathrm{T}}|\rangle$ generated in the RC

$$V_{dm}(f_p) = \frac{\langle|E_T|\rangle}{\langle|E_T^{1W}(f_p)|\rangle}.V_{dm}^{1W}(f_p) \tag{5}$$

with $\langle|E_T^{1W}(f_p)|\rangle$ the average total electric field strength which would be obtained for a forward power P_f of 1 W. This DM voltage $V_{dm}(f_p)$ can then be added to the useful signal $s_u(t)$ in the time-domain as it is well-known that in many cases, and particularly in the case of TWP, the useful signal is transmitted using the DM. This is done in the fourth and last step of the method which consists in verifying the integrity of a given useful signal $s_u(t)$ (generated numerically) after superimposing the amplitude of the CW disturbance at the frequency f_p which is related to the magnitude of $V_{dm}(f_p)$. As this latter metric is calculated for each mode stirrer position, the disturbed signal $s_d(t)$ can be calculated for instance for each stirring configuration, for the worst stirring configuration (i.e. "worst case") or also from an average of the disturbance obtained for all the configurations. As mentioned earlier, the parasitic signal is a sinusoidal signal at the frequency f_p, so it can be defined as follows

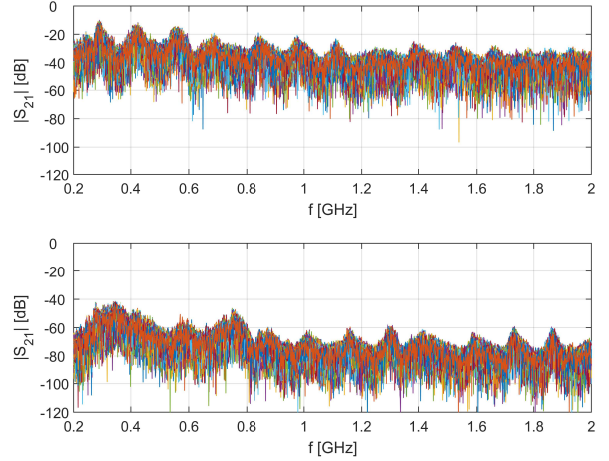$$s_p(t) = |V_{dm}(f_p)|\cos(2\pi f_p t + \varphi) \tag{6}$$

Fig. 6. Magnitude of the S_{21} parameter for all the mode stirrer positions in the unloaded RC for the unshielded TWP (top subplot) and the shielded one (bottom subplot) of 1 m length.
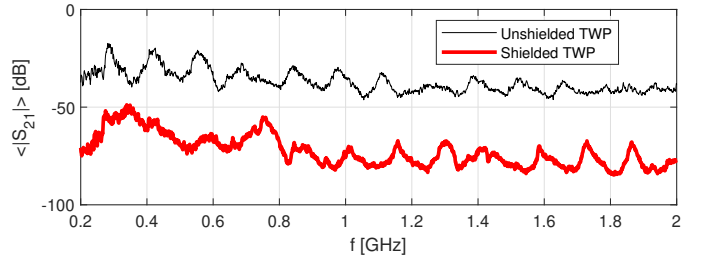

Fig. 7. Comparison of the average magnitude of S_{21} over all the mode stirrer positions in the unloaded RC for the unshielded and the shielded TWP of 1 m length.

with φ a value generated randomly between 0 and 2π.

The in-depth analysis of the disturbed signal $s_d(t)$ allows its signal integrity to be verified. This process can also be repeated for any set of input parameters (i.e. f_p, $\langle|E_{\mathrm{T}}|\rangle$ and τ) provided that f_p is a frequency where the S-parameters have been measured. As seen later, it is worth noting that the metrics of interest used to judge the signal integrity are dependent of the useful signal.

E. Results

1) S-parameter measurements: Before performing virtual signal integrity tests, it is interesting to analyze carefully the S-parameter measurements obtained for both TWPs. Fig. 6 presents the comparison of the S_{21} magnitude measured for all the mode stirrer positions in the unloaded RC for the unshielded and the shielded TWP of 1 m length. As shown in Fig. 7 where the average is plotted, the level of coupling is, as expected, decreased of roughly 40 dB (on average) on the whole frequency range in the case of the shielded TWP. Fortunately, this level is higher than the noise floor of the VNA measurements (assumed to be around -110 dB in these measurement conditions). It makes sense to consider that this average difference of coupling depends of the TWP length. This is shown in Fig. 8 for 3 lengths (i.e. 50, 75 and 100 cm) of both the unshielded and the shielded TWPs.
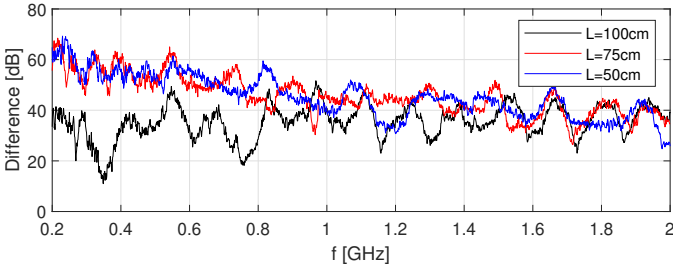
Fig. 8. Comparison of the average difference of magnitude of the S_{21} parameter for the unshielded and the shielded TWP over all the mode stirrer positions in the unloaded RC for 3 different lengths of the TWPs.
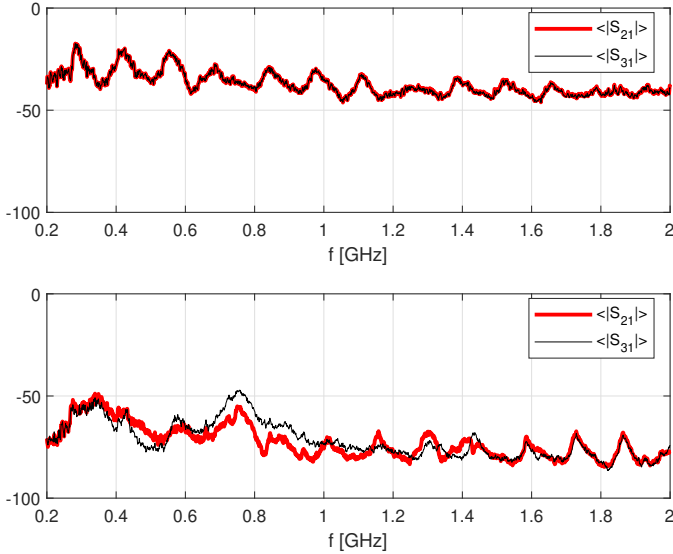

Fig. 9. Comparison of the average magnitude of S_{21} and S_{31} (expressed in dB) over all the mode stirrer positions in the unloaded RC for the unshielded TWP (top subplot) and the shielded one (bottom subplot).
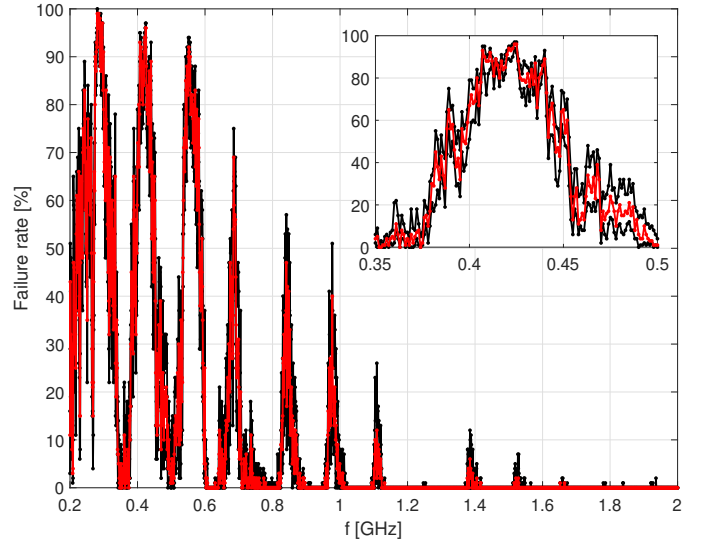

Fig. 10. Failure rate obtained on the unshielded TWP of 1 m length for the unloaded RC and for the first position of the emitting antenna (for $\langle |E_T| \rangle$ = 100 V/m and τ = 0 dB). The red plot corresponds to the results obtained for $\langle |E_T| \rangle$ = 100 V/m while black plots are related to $\langle |E_T^{min}| \rangle$ and $\langle |E_T^{max}| \rangle$. The inset is a zoom between 0.35 and 0.5 GHz.

As in [12], it is important to verify that the devoted PCB is perfectly balanced on the whole frequency range of interest. This is proven in Fig. 9 where the average of S_{21} and S_{31} are shown to be identical in the case of the unshielded TWP of 1 m length. The slight difference observed in the case of the shielded TWP is assumed to be related to the non uniformity of the cross section geometry of the TWP in reason of the presence of the braided shield and the aluminum foil.

2) Example of Signal Integrity Test: As mentioned earlier, many different metrics can be used as an output of the proposed method. In this subsection, we illustrate the relevance of the method on a simple square useful signal defined by a high level A_u of 1 V and a low level $-A_u$ (note that the frequency of the square signal has no influence on the results presented in this section).

The signal integrity of the disturbed signal $s_d(t)$ is then verified for any mode stirrer position and any parasitic frequency f_p for a total average electric field strength $\langle |E_T| \rangle$ of 100 V/m. A loss of signal integrity is here defined as follows : when $s_d(t)$ is lower than 0 when $s_u(t) > 0$ and vice versa. In concrete terms, a failure is obtained when $V_{dm}(f_p) > A_u$ (i.e. 1 V). For each frequency f_p, a failure rate is calculated as the ratio of the number of mode stirrer positions leading

to a loss of signal integrity and the total number of mode stirrer positions (i.e. N = 100). When calculating the results, it is also interesting to consider the uncertainty related the method. As most of the method is done in post-processing, we can assume that the main factor of uncertainty lies in the difference between the desired value of $\langle |E_T| \rangle$ and the real value which would be obtained in the RC (which is unknown) for the transmitted power P_t^{cor}. We can indeed assume here that the uncertainty related to the S-parameters measurements is negligible with respect to this latter source of uncertainty.

The uncertainty of the EM field strength within the RC can be considered easily as follows. For instance, when the results of the method are computed for $\langle |E_T| \rangle$, one just needs to consider that the same results are obtained also for $\langle |E_T^{min}| \rangle$ and $\langle |E_T^{max}| \rangle$, these latter values being calculated thanks to a given level of uncertainty σ expressed in dB. As an example, the results shown in the following have been calculated for $\langle |E_T| \rangle$ = 100 V/m (i.e. 40 dBV/m) and σ = 1.5 dB (i.e. $\langle |E_T^{min}| \rangle$ and $\langle |E_T^{max}| \rangle$ equal respectively 84.1 V/m and 118.9 V/m or 38.5 and 41.5 dBV/m). This means in concrete terms that, instead of having $\langle |E_T| \rangle$ = 100 V/m, this value is in reality included between 84.1 V/m and 118.9 V/m if σ equals 1.5 dB.

The results shown hereafter have been calculated for two different positions of the antenna within the RC and both loading conditions presented earlier. The comparison made in Fig. 11 of the power P_t^{cor} to inject in order to obtain $\langle |E_T| \rangle$ = 100 V/m shows that this value is independent of the position of the antenna within the RC for a given loading condition. This power has to be increased (of around 1.5 dB) over the whole frequency range in the case of the loaded RC in order to compensate the additional losses due to the block of absorber.

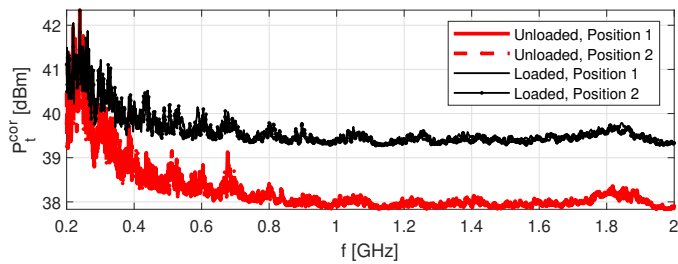Fig. 10 presents the failure rate obtained on the 1 m long

Fig. 11. Comparison of the transmitted power P_t^{cor} required to obtain $\langle |E_\mathrm{T}| \rangle$ = 100 V/m in the RC for both positions of the emitting antenna and both loading conditions.
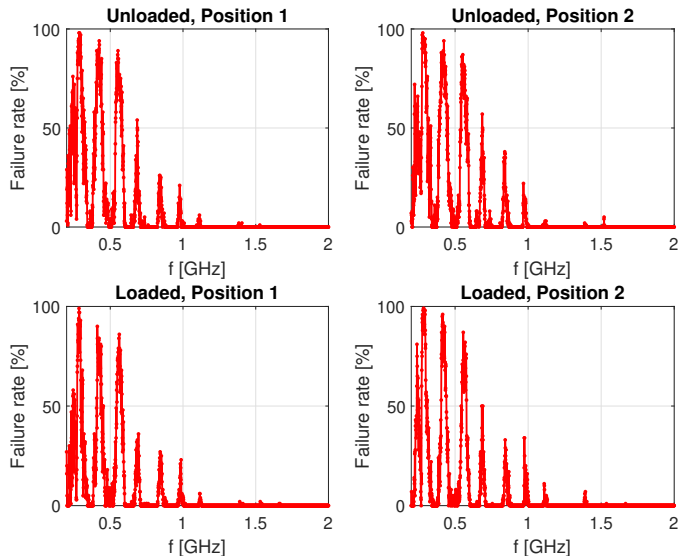

Fig. 12. Failure rate obtained on the unshielded TWP of 1 m length for two different positions of the antenna and both loading conditions (for $\langle |E_\mathrm{T}| \rangle$ = 100 V/m and τ = 0 dB).

TABLE I
CM IMPEDANCE CONFIGURATIONS USED ON TERMINATION 2 OF THE TWP

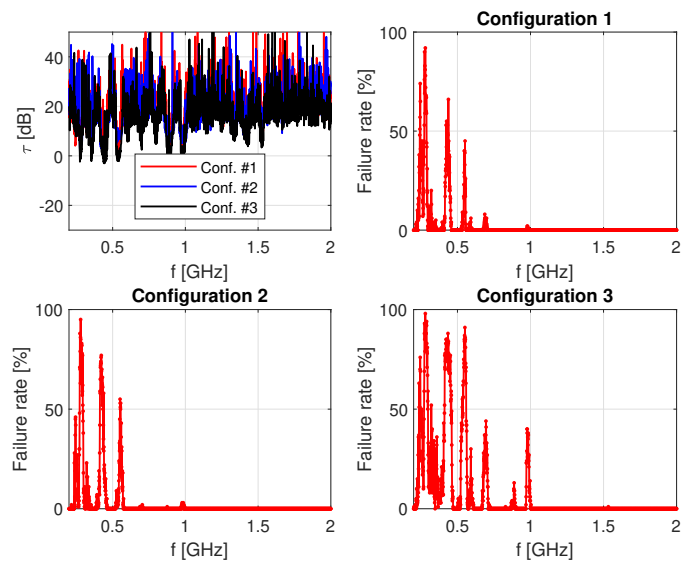| Configuration	Z_{cm3}	Z_{cm4}
1	50 Ω	Open circuit
2	50 Ω	Short circuit
3	Open circuit	Short circuit

Fig. 13. Comparison of the common-mode rejection rate τ (top, left) and failure rate obtained on the unshielded TWP of 1 m length in the unloaded RC for the three common-mode impedance configuration described in Table I ((for $\langle |E_\mathrm{T}| \rangle$ = 100 V/m).

unshielded TWP in the case of the unloaded RC for τ = 0 dB and for the first position of the emitting antenna. It is clear that these results are strongly dependent of the TWP length. Indeed, a high failure rate is directly related to a frequency when the TWP is resonating (i.e. roughly when the length L is a multiple of $\lambda/2$ with λ being the wavelength). This is the case for instance for the first peak of the failure rate observed around 290 MHz when the TWP length is close to λ. These results are therefore consistent with the S-parameters shown in Fig. 7. Indeed, it is clear that a higher level of S_{21} coupling leads to a high failure rate in the virtual signal integrity test. The second main conclusion lies in the fact that the variation of the failure rate as a function of the uncertainty on $\langle |E_\mathrm{T}| \rangle$ is really low even when considering an uncertainty level σ of 3 dB (± 1.5 dB), a typical level of uncertainty considered in a RC. It is worth noting that the failure rate is null on the whole frequency range for the shielded TWP for the same values of $\langle |E_\mathrm{T}| \rangle$ and τ.

The same results can be calculated for both positions of the emitting antenna and both loading conditions. The comparison in Fig. 12 of the failure rate clearly shows that it is similar for each measurement configuration, provided that the RC is well-stirred. Indeed, the lower level of S_{21} coupling obtained in

the loaded RC is compensated by the greater power $P_{cor}(f_p)$ supplying the antenna for this configuration.

In addition to these results obtained in a "perfect" balanced configuration, other results have been obtained after measuring the S-parameters with CM loading terminations Z_{cm3} & Z_{cm4} (i.e. at Termination 2 of the TWP) described in Table I. For these unbalanced configurations, S_{21} and S_{31} are different and the magnitude of V_{dm} can be calculated directly (as well as τ which is here frequency-dependent) by calculating the difference between the magnitude of both CM voltages.

The results presented in Fig. 13 first show that the value of τ = 0 dB selected before is not so far from the values obtained in these configurations which are here around (on average) 20 dB. Second, it is shown that the failure rate is related to τ which is different for each unbalanced termination loads. Indeed, the failure rate is, for most of the frequencies, higher for the configuration 3 (which makes sense as both impedances are extreme) when τ is generally lower.

As a conclusion on this section, it is important to remind once again that different useful signals could be considered as well as different outputs metrics (for instance the eye-diagram as shown in [12]).

III. IMPROVEMENT OF THE METHOD TO DEAL WITH REALISTIC INDUSTRIAL CONSTRAINTS

A. Limitations of the Previous Approach

The method presented in [12] in a BCI context and extended to the case of RCs in the first part of this paper suffers of several assumptions and simplifications which decreases the representativity of the method with respect to real industrial constraints.

First, the outputs of the method are obtained for a given length of the TWP under test, i.e. the length of the TWP used during the S-parameter measurements. Indeed, this length drives the current distribution (and specifically the resonances) on both wires of the TWP and on the shield in the case of the shielded one. It is therefore not trivial to extrapolate the obtained results to the case of a similar TWP having a different length.

Second, the considered value of the CMRR τ is independent of the frequency which does not represent the reality. This effect has been shown in Fig. 13) when the measured CMRR is shown to exhibit some variations with the frequency.

Third, the CM termination loads on each wire of the TWP (in the termination where the S-parameters are measured) are balanced and equal to 50 Ω. In a real application, the impedance presented by an electronic equipment on each input pin may be different and potentially frequency-dependent.

B. Principle of the Improved Approach

The method is improved in this second part in order to solve the limitations of the previous approach and therefore to deal with realistic industrial constraints. This is done with the help of numerical simulations performed in our paper (without loss of generality) with the full-wave professional simulation software called FEKO [24]. This well-known software uses the method of moments to solve the Maxwell's equations in the frequency domain.

Provided that the numerical model is sufficiently accurate and the CM termination loads are known on a large frequency range (for instance if they are given by the equipment supplier or if they have been measured), the method can be applied without requiring any measurements (for the unshielded TWP). As just mentioned, this implies that the numerical model is sufficiently accurate. This is why it is investigated in the next subsection.

C. About the Full-wave Model Accuracy

The aim of the numerical simulations done in this improved approach are to show that, in the case of the unshielded TWP, the simulations are able to match the measurements. Indeed, a sufficiently accurate model of the TWP could lead us to assume that the S-parameter measurements are no longer required (for the unshielded TWP only, as shown before).

To reach this ambitious objective, we have tried, as shown in Fig. 14 to reproduce faithfully on the frequency range 10 MHz to 2 GHz the experiment described in Fig. 1 in the case of the unshielded TWP located above a ground plane and connected to two metallic brackets. It is worth noting that the shielded
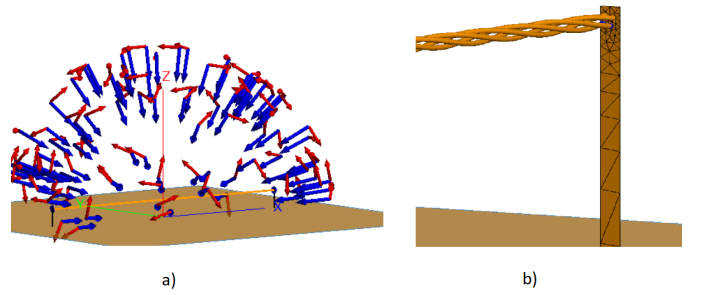

Fig. 14. Picture of full-wave simulations (using FEKO) showing a) the TWP located above an infinite ground plane and excited by a given spectrum of 50 plane waves and b) a zoom on a termination of the TWP. Note that the four conductors of the cable constituting both TWPs have been reproduced for a better accuracy, the second one being left unconnected.

TWP has not been modelled numerically in reason of the hardness to reproduce accurately the braided shield as well as the aluminum foil.

In order to reduce the required computation times, some assumptions have been considered. First, both metallic brackets of 52 mm height and 3 mm width are smaller than the ones used in measurements. Second, the devoted PCB described before has not been considered in our numerical model, both wires of the TWP being directly connected to a CM load. Third, the outer dielectric coating (but not the one surrounding each conductor) has also been neglected in these simulations. Fourth, the ground plane has been modelled as a perfect electric conductor of infinite dimensions. Finally, the Faraday cage and the antenna have not been considered in the modelings. Instead, each position of the mode stirrer is represented through the summation of n plane waves in free space as proposed initially in [25]. This approach is interesting as $\langle |E_T| \rangle$ is directly related to the amplitude of the plane waves E_0 and to the number n of plane waves considered for each spectrum

$$\langle |E_T| \rangle = E_0 \sqrt{n} \frac{15}{16} \sqrt{\frac{\pi}{3}} \qquad (7)$$

In this paper, we have chosen to consider $N = 50$ plane wave spectrum (each representing one mode stirrer position), each spectrum being constituted of $n = 50$ plane waves of equal magnitude E_0. These values would lead to $\langle |E_T| \rangle = 100$ V/m. However, equation (7) is valid only when the EM field is related to the summation of plane waves propagating in free space and not close to a metallic ground plane [26]. In order to better represent the reality, we have preferred to compute, again from FEKO simulations, the average magnitude of the total electric field obtained over 100 points, each of them being located at a distance of 5 cm from the ground by 50 other plane wave spectrum having the same characteristics. Therefore, for each frequency of interest, the DM voltage which would be obtained for $\langle |E_T| \rangle = 100$ V/m can be calculated easily in a similar manner than what is done in equation (5).

Fig. 15 presents a comparison of the average CM voltage induced at the termination of the TWP of 1-m length obtained in measurements and in simulation for a balanced load configuration and $\langle |E_T| \rangle = 100$ V/m. This figure exhibiting slight
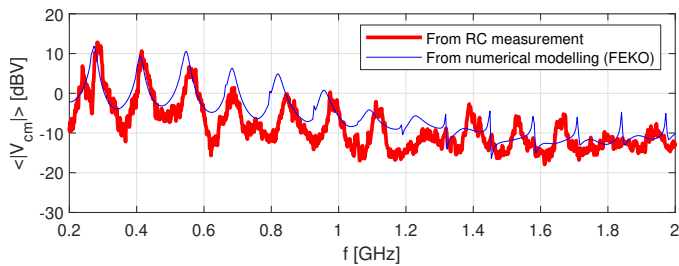
Fig. 15. Comparison of the CM voltage obtained on a 50 Ω load in a balanced configuration from RC measurements and in Simulations (FEKO) for $\langle |E_T| \rangle$ of 100 V/m on an unshielded TWP of 1 m length.

TABLE II
VALUES OF THE RLC PARALLEL CIRCUIT ELEMENTS USED IN
SIMULATION

	Z_{cm1}	Z_{cm2}	Z_{cm3}	Z_{cm4}
R [Ω]	200	500	500	400
L [nH]	35	80	240	120
C [pF]	6	13	20	1

differences between measurements and simulations (and in particular a slight overestimation of the simulated results of no more than 3 dB) implies that it is possible to be reasonably confident with the fact that the simulated results represents satisfyingly the measurements. Indeed, we can assume that the simplifications of the numerical model mentioned above can explain the differences obtained between measurements and simulations.

Once the numerical model assumed to be validated, it becomes possible in simulations to connect at each extremity of both wires constituting the TWP any value of the termination loads and possibly frequency-dependent ones (and unlike S-parameter measurements which are done with 50 Ω loads connected on each VNA port). Then, the method can be applied directly on the differential voltage V_{dm} calculated at one termination of the (unshielded) TWP under investigation with a good confidence on the accuracy of the results.

D. Signal Integrity Results

1) Results for the Unshielded TWP: The improved method has been applied on the numerical model of the unshielded TWP presented before and loaded with frequency-dependent CM impedances (each represented by a RLC parallel circuit) described in Table II. These values have been chosen to be representative of the industrial automotive context in order to illustrate the relevance of the improved approach.

The useful signal has been generated following the Fast Ethernet protocol 100BASE-T1, where the data are transmitted in "full-duplex" mode using a TWP. This protocol uses the 3PAM (with PAM meaning "pulse amplitude modulation") where 3 bits are converted in 2 symbols, each symbol having 3 possible values of -1 V, 0 V and +1 V. More accurately, 100000 bits have been generated numerically using this protocol with a data symbol rate of 66.7 MHz. This discrete signal has then been converted in a continuous one thanks to a raised-cosine filter as requested by the protocol. The aim of generating such
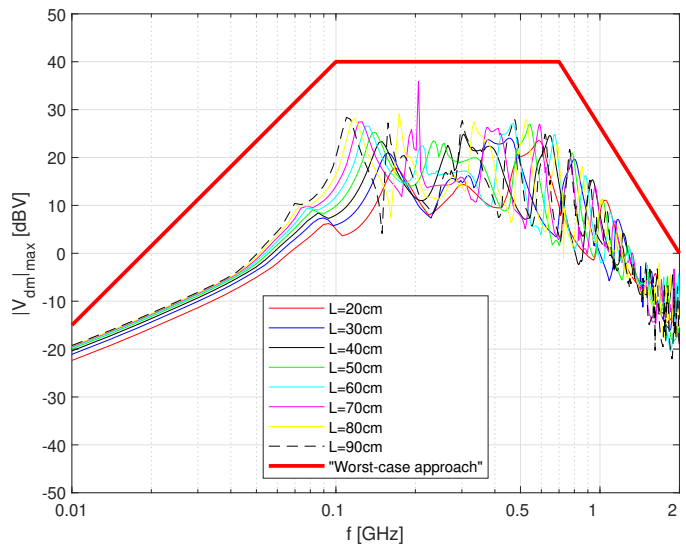

Fig. 16. Comparison (from FEKO simulations) of the maximum DM voltage obtained for all the plane wave spectrum in the unbalanced configuration on 8 unshielded TWPs of different lengths (for $\langle |E_T| \rangle$ of 100 V/m). The thick line could correspond to the level considered in the case of a typical EMC study based on a "worst-case approach" guaranteeing a safety margin of a few dB.

large number of bits is to be able to compute a bit-error-rate (BER) of the virtually received useful signal, i.e. a ratio of the number of wrong bits received divided by the total number of bits, when the TWP is exposed in a RC [27].

This has been done following the computation of the magnitude of V_{dm} obtained on the unshielded TWP model for different lengths of the TWP (from 20 to 90 cm with a step of 10 cm), each loaded by the CM impedances described in Table II. The addition of a harmonic disturbance would lead for a given configuration to almost "binary" results (i.e. loss/no loss of signal integrity) as shown in section III. Therefore, in order to obtain low BER values, the disturbance signal is here the sum of 2 CW disturbances (of frequencies 300 and 370 MHz) having again an amplitude related to the magnitude of V_{dm} at the corresponding frequencies.

The maximum DM voltage obtained at each frequency for all the spectrum and for each unshielded TWP is plotted in Fig. 16. It is clear from that figure that, even if the specific resonances are always different for each TWP, the general trend is similar for all the TWPs.

Fig. 17 presents the bits of the useful signal (and the associated continuous signal) as well as the sampled signal (from the corresponding continuous one) after application of the disturbance for the unshielded TWP of 90 cm long in the case of $\langle |E_T| \rangle$ = 100 V/m. Then, the BER can be calculated after analyzing if each bit has been correctly received. To do this, any sampled value greater than +0.5 V is assumed to be a +1 V symbol, a value lower than -0.5 V to be a -1 V symbol and all the values included in the range between -0.5 V and +0.5 V are associated to a 0 V symbol. Under these conditions, it is clear that this level of disturbance involves a visible signal integrity loss.

To deepen the analysis, the BER calculated from the simulated results on the 8 unshielded TWPs of different lengths
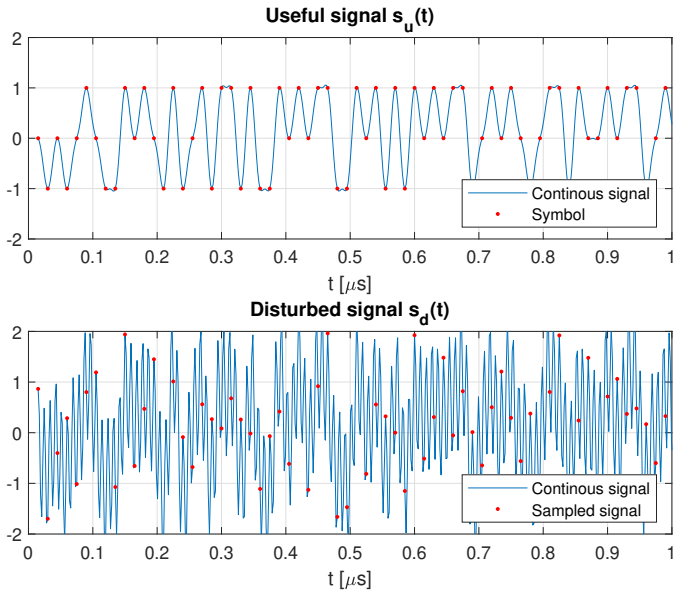
Fig. 17. Time-domain waveform (over 1 μs) of the useful 100BASE-T1 signal $s_u(t)$ and of the disturbed signal $s_d(t)$. The parasitic signal is the sum of 2 harmonic disturbances of 300 and 370 MHz calculated from the maximum value of V_{dm} in the case of the unshielded TWP of length 90 cm (for $\langle|E_T|\rangle$ of 100 V/m).
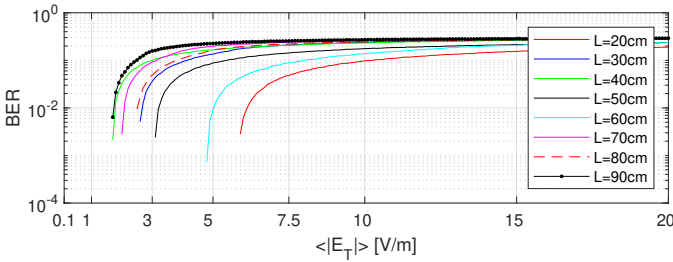

Fig. 18. Bit-error-rate (BER) as the function of $\langle|E_T|\rangle$ obtained on the 100BASE-T1 signal from numerical simulations on unshielded TWPs of different lengths. The computation is made on the maximum value of V_{dm} calculated at each frequency over the 50 simulations. The parasitic signal is the sum of 2 harmonic disturbances of 300 and 370 MHz.

is plotted in Fig. 18 as a function of $\langle|E_T|\rangle$. As expected, the BER depends directly of the TWP length which drives the current distribution all along both wires of the TWP and as a consequence drives the differential voltage V_{dm} at any frequency of interest. The first error in the data transmission is observed around $\langle|E_T|\rangle$ = 5.9 V/m for the 20 cm TWP while a BER of 10^{-2} is reached at $\langle|E_T|\rangle$ = 3.2 V/m for the 50 cm long TWP. It is worth noting that lower BER values could be obtained in the case of the generation of a larger number of bits.

2) Results for the Shielded TWP: As mentioned previously, the shielded TWP has not been simulated. However, the improved approach can still be applied after combining numerical and experimental results. The solution consists in considering the differential voltage $V_{dm}(f_p)$ calculated on the simulated unshielded TWP and to apply on this result the shielding attenuation D obtained in the S-parameter measurements between unshielded and shielded TWP. D is defined as follows
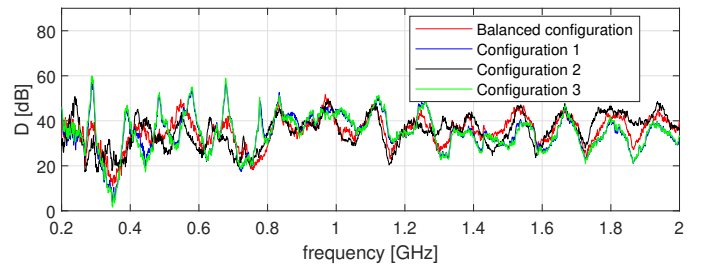

Fig. 19. Comparison of D (in dB) obtained for 4 different loading configurations for the 1 m length unshielded and shielded TWPs.
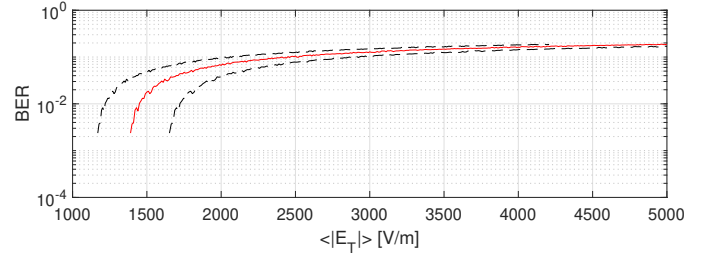

Fig. 20. Bit-error-rate (BER) as the function of $\langle|E_T|\rangle$ obtained on the 100BASE-T1 signal from numerical simulations on the shielded TWP of 50 cm length. The computation is made on the maximum value of V_{dm} calculated at each frequency over the 50 simulations. The parasitic signal is the sum of 2 harmonic disturbances of 300 and 370 MHz. The BER is also plotted for an uncertainty on $\langle|E_T|\rangle$ of ± 1.5 dB (dashed line).

$$D = \langle|S_{21}^{uns}|\rangle / \langle|S_{21}^{sh}|\rangle \qquad (8)$$

with the superscripts "uns" and "sh" meaning respectively unshielded and shielded.

This approach requires therefore that the S-parameter measurements described in Fig. 1 have been performed on both TWPs having the same length than the unshielded TWP which has been simulated. Indeed, it seems difficult to extrapolate the value of D which would be measured for TWP of different lengths. This approach aims at considering that the attenuation related to the shield is similar whatever the terminal conditions of the TWP. In order to prove this assumption, Fig. 19 presents the comparison of D (in dB) from the measurements done on the 1-m long TWP for the balanced configuration and the three unbalanced ones described in Table I. The presented results clearly show, despite some slight differences, that this assumption seems to be valid. The differential voltage V_{dm} for the shielded TWP can then be calculated after multiplying D to the differential voltage calculated on the simulated unshielded TWP (i.e. $\left|V_{dm}^{sh}\right| = |V_{dm}^{uns}|/D$). It is therefore simple to compute the BER obtained for the shielded TWP.

Fig. 20 presents the BER obtained on the shielded TWP of 50 cm long for the configuration described previously for the unshielded TWPs. As a matter of comparison, the calculated BER reaches 10^{-2} for $\langle|E_T|\rangle$ = 1450 V/m, which corresponds to a gain of 53.1 dB with respect to the unshielded TWP of same length. The BER has also been plotted after considering an uncertainty of $\langle|E_T|\rangle$ of ± 1.5 dB.

IV. CONCLUSION

The method presented in [12] and able to realize "virtual" signal integrity tests on TWPs using a BCI setup has been extended in this paper to the case of RCs.

The first part of the manuscript has presented the adaptation of the method to the characteristics of this EMC testing facility in order to extend towards higher frequencies the frequency range of the method application. The method entirely done in post-processing with the exception of the S-parameter measurements presents the advantages to be applicable for any type of digital communication and for any metrics related to a signal integrity test (failure rate, eye-diagram and BER for instance). The method, proven to be independent of the measurement conditions (position of the antenna and of the TWP within the RC, Q-factor) provided that the RC is well-stirred, can take advantage of the results obtained for each stirring configuration. The method would give therefore reliable data to the automotive suppliers in order to decide if a shielded TWP is required in a given situation or if an unshielded one can be sufficient. It has also been shown that the method can easily take into account the uncertainty related to the average EM field strength generated in the RC.

In the second part of the manuscript, the method has been enriched with the help of numerical simulations in order to deal with real industrial constraints. This solution does not require anymore to consider a frequency constant CMRR. In case of sufficiently accurate numerical simulations, the improved method is therefore able, in the case of unshielded TWPs, to deal with frequency-dependent terminal impedances as well as any length of the TWP without any measurements required. For shielded TWPs, S-parameter measurements performed on unshielded and shielded TWP of same length than the unshielded TWP considered in simulations are still needed in order to apply the attenuation provided by the shield on the unshielded TWP numerical results. It should be emphasized here that the improved approach could be also applied in a similar manner from experiments performed using a BCI setup. It is also worth noting that the method applied over TWPs could also be applied similarly on any communication link made of a pair of conductors.

This manuscript has presented the application of the method under a deterministic aspect, that is to say by trying to reduce as much as possible all the possible sources of error in order to obtain accurate results. This approach is not generally the approach used in the industry where one rather seeks, generally from measurements but sometimes also from simulations, 1) to simplify the analysis by taking a margin of a few dB, as it is shown for instance with the thick curve plotted in Fig. 16, and 2) to increase the confidence in the obtained results. It is important to note here that the proposed method can be used easily with this kind of "worst-case" approach, which in our opinion reinforces its relevance.

REFERENCES

[1] "Ieee draft standard for ethernet physical layer specifications and management parameters for greater than 1 gb/s automotive ethernet," *IEEE P802.3ch/D3.2, February 2020*, pp. 1–215, 2020.

[2] S. Mortazavi, D. Schleicher, and F. Gerfers, "Characterization and verification of gigabit ethernet-based bus systems in vehicles," in *2018 IEEE International Symposium on Electromagnetic Compatibility and 2018 IEEE Asia-Pacific Symposium on Electromagnetic Compatibility (EMC/APEMC)*, 2018, pp. 428–433.

[3] P. DeRoy, N. Toscani, F. Grassi, W. Schulz, and C. Rostamzadeh, "Sensitivity analysis of rf current injection techniques for immunity testing of automotive ethernet," in *2018 IEEE Symposium on Electromagnetic Compatibility, Signal Integrity and Power Integrity (EMC, SI PI)*, 2018, pp. 461–466.

[4] S. Jeschke, A. H. Razavi, J. Loos, and J. Baerenfaenger, "Impact of hv battery cables' emissions on the signal integrity of 2-wire ethernet communication in automotive application," in *2019 International Symposium on Electromagnetic Compatibility - EMC EUROPE*, 2019, pp. 754–758.

[5] "Metallic communication cable test methods - part 4-15: Electromagnetic compatibility (emc) - test method for measuring transfer impedance and screening attenuation - or coupling attenuation with triaxial cell," *IEC 62153-4-15:2015*, December 2015.

[6] "Metallic communication cable test methods: Part 4-6: Emc – surface transfer impedance - line injection method," *IEC 62153-4-6*, May 2006.

[7] B. Démoulin and L. Koné, "Shielded cable transfer impedance measurements," *IEEE-EMC Newsletter*, pp. 30–37, Fall 2010.

[8] Z. E. M. Chérif, G. Andrieu, G. Alberto, N. Ticaud, C. Jullien, J. Genoulaz, and A. Dieudonné, "Transfer impedance measurement of shielded cables through localized injection," *IEEE Transactions on Electromagnetic Compatibility*, vol. 60, no. 4, pp. 1018–1021, Aug 2018.

[9] E. D. Knowles and L. W. Olson, "Cable shielding effectiveness testing," *IEEE Transactions on Electromagnetic Compatibility*, vol. EMC-16, no. 1, pp. 16–23, 1974.

[10] V. M. Primiani, F. Moglie, and A. P. Pastore, "Modeling of the reverberation chamber method for determining the shielding properties of a coaxial cable," *IEEE Transactions on Electromagnetic Compatibility*, vol. 50, no. 2, pp. 246–251, May 2008.

[11] B. Démoulin and L. Koné, "Shielded cable transfer impedance measurements high frequency range 100 mhz - 1 ghz," *IEEE-EMC Newsletter*, pp. 42–50, Spring 2011.

[12] S. Rasm, G. Andrieu, A. Reineix, and R. Tumayan, "Virtual signal integrity test on shielded/unshielded twisted-wire pairs using the bulk current injection setup," *IEEE Transactions on Electromagnetic Compatibility*, vol. 63, no. 5, pp. 1357–1365, 2021.

[13] "Integr. circuits – meas. electromagn. immunity, 150 khz to 1 ghz - part 3: Bulk current injection (bci) method," *IEC 62132-3*, 2007.

[14] Jian Zhou and Jin Liu, "On the measurement of common-mode rejection ratio," *IEEE Transactions on Circuits and Systems II: Express Briefs*, vol. 52, no. 1, pp. 49–53, 2005.

[15] F. Grassi, F. Marliani, and S. A. Pignari, "Circuit modeling of injection probes for bulk current injection," *IEEE Transactions on Electromagnetic Compatibility*, vol. 49, no. 3, pp. 563–576, Aug 2007.

[16] F. Grassi and S. A. Pignari, "Immunity to conducted noise of data transmission along dc power lines involving twisted-wire pairs above ground," *IEEE Transactions on Electromagnetic Compatibility*, vol. 55, no. 1, pp. 195–207, 2013.

[17] M. Höijer, "Maximum power available to stress onto the critical component in the equipment under test when performing a radiated susceptibility test in the reverberation chamber," *IEEE Transactions on Electromagnetic Compatibility*, vol. 48, no. 2, pp. 372–384, May 2006.

[18] G. Andrieu, N. Ticaud, and F. Lescoat, "On the risk to declare emc compliant a faulty eut during radiated susceptibility tests in reverberation chambers," *IEEE Transactions on Electromagnetic Compatibility*, vol. 62, no. 3, pp. 645–653, 2020.

[19] G. Andrieu, "Risk to declare emc compliant a faulty eut during radiated susceptibility tests performed in an undermoded reverberation chamber," *IEEE Transactions on Electromagnetic Compatibility*, vol. 63, no. 2, pp. 365–374, 2021.

[20] A. Adardour, G. Andrieu, and A. Reineix, "On the low-frequency optimization of reverberation chambers," *IEEE Transactions on Electromagnetic Compatibility*, vol. 56, no. 2, pp. 266–275, April 2014.

[21] P. S. Kildal, X. Chen, C. Orlenius, M. Franzen, and C. S. L. Patane, "Characterization of reverberation chambers for ota measurements of wireless devices: Physical formulations of channel matrix and new uncertainty formula," *IEEE Transactions on Antennas and Propagation*, vol. 60, no. 8, pp. 3875–3891, Aug 2012.

[22] P. Besnier, C. Lemoine, and J. Sol, "Various estimations of composite q-factor with antennas in a reverberation chamber," in *2015 IEEE International Symposium on Electromagnetic Compatibility (EMC)*, Aug 2015, pp. 1223–1227.

[23] G. Andrieu, N. Ticaud, F. Lescoat, and L. Trougnou, "Fast and accurate assessment of the "well stirred condition" of a reverberation chamber from s_{11} measurements," *IEEE Transactions on Electromagnetic Compatibility*, vol. 61, no. 4, pp. 974–982, Aug 2019.

[24] "Feko software," *Website : https://altairhyperworks.com/product/feko*.

[25] L. Musso, V. Berat, F. Canavero, and B. Demoulin, "A plane wave monte carlo simulation method for reverberation chambers," in *Proc. Eur., Int. Symp. Electromagn. Compat.y*, vol. 1, no. 3, 2002, pp. 45–50S.

[26] D. A. Hill, "Boundary fields in reverberation chambers," *IEEE Transactions on Electromagnetic Compatibility*, vol. 47, no. 2, pp. 281–290, May 2005.

[27] E. Genender, C. L. Holloway, K. A. Remley, J. M. Ladbury, G. Koepke, and H. Garbe, "Simulating the multipath channel with a reverberation chamber: Application to bit error rate measurements," *IEEE Transactions on Electromagnetic Compatibility*, vol. 52, no. 4, pp. 766–777, Nov 2010.